Improvement of accuracy in ultrasonic measurement of luminal surface roughness of carotid arterial wall by deconvolution filtering

Yoshifumi Nagai[1], Hideyuki Hasegawa[1,2], and Hiroshi Kanai[1,2]*

[1]Graduate School of Biomedical Engineering, Tohoku University, Sendai 980-8579, Japan
[2]Graduate School of Engineering, Tohoku University, Sendai 980-8579, Japan
E-mail: kanai@ecei.tohoku.ac.jp

The diagnosis of early-stage atherosclerosis is important for preventing cardiovascular diseases such as a stroke or a heart attack. The main cause of such diseases is atherosclerosis. In early-stage atherosclerosis, the luminal surface of the arterial wall becomes rough because of the detachment of endothelial cells and the degeneration of the internal elastic layer. Therefore, it would be useful if the minute luminal surface roughness of the carotid arterial wall observed in the early stage of atherosclerosis can be measured noninvasively by ultrasonography. In conventional ultrasonography, the axial resolution of a B-mode image depends on the ultrasonic pulse length of 150 µm (at 10 MHz) because a B-mode image is constructed using the amplitude of the RF echo. However, the thickness of an endothelial cell covering the luminal surface is 10–20 µm. Therefore, a minute surface roughness cannot be measured from a conventional B-mode image. We have realized the transcutaneous measurement of such a minute surface roughness of about 10 µm using the phased-tracking method. However, the lateral spatial resolution degrades owing to the point spread function (PSF) because the diameter of an ultrasonic beam is finite. In the present study, we proposed a method of improving the lateral spatial resolution in the estimation of surface roughness using a Wiener filter to suppress the effect of the PSF of the ultrasound system employed. The proposed method was validated using a phantom and then applied to the in vivo measurement of carotid arteries. © 2014 The Japan Society of Applied Physics

1. Introduction

Circulatory diseases are considered to be mainly caused by atherosclerosis. Therefore, the early diagnosis and prevention of atherosclerosis are important. Medical ultrasonography is widely used for diagnosis and treatment in clinical situations. Diagnostic ultrasound is noninvasive and, thus, can be repeatedly employed. Such properties of diagnostic ultrasound is suitable for the diagnosis of atherosclerosis because the progress of atherosclerosis requires long-term monitoring.[1–8]

In the early stage of atherosclerosis, the internal elastic layer and endothelial cells are damaged, leading to the detachment of endothelial cells and the degeneration of the internal elastic layer.[9,10] As a result, the luminal surface of the arterial wall becomes rough.[11–13] Therefore, it is important for the diagnosis of atherosclerosis in its early stage to measure such a minute luminal surface roughness of the arterial wall. The luminal surface is covered with endothelial cells, and an endothelial cell is 10–20 µm thick.[14] Therefore, a high spatial resolution on the micron order is required, since such a minute roughness cannot be measured by conventional ultrasonography whose spatial resolution is about 0.1 mm at 10 MHz of ultrasonic center frequency. Arihara et al. measured the micron-order surface profile of an object made of silicone rubber using the phase shift of RF echoes during a sweep of an ultrasonic beam.[15] However, in their method, the luminal surface cannot be measured accurately in vivo because of the movement of the arterial wall in the axial (arterial radial) direction due to pulsation.

In recent years, owing to significant improvements in the performance of ultrasonic diagnostic equipment, the movement of the arterial wall not only in the arterial radial direction but also in the longitudinal direction have been observed in a B-mode image.[16] This longitudinal movement is considered to be caused by the contraction of the heart. Cinthio et al. suggested the measurement of a minute roughness using this arterial wall movement in the arterial

longitudinal direction without sweeping an ultrasonic beam.[17,18] In this method, the phased-tracking and block matching methods are used to measure the displacements of the luminal surface caused by surface roughness and the increase in arterial diameter during a cardiac cycle. In Cinthio et al.'s validation experiments, the surface profile of silicone phantoms, which had a roughness of 13–33 µm height, was measured. It was shown that a minute surface roughness could be measured by ultrasound. However, the movement of the arterial wall in the longitudinal direction is small (less than 1 mm) and, thus, the length of a region measured using an ultrasonic beam is limited. Therefore, Kitamura et al. expanded the measured region by combining multiple surface profiles measured by multiple ultrasonic beams.[19]

In Kitamura et al.'s measurement, the micron-order spatial resolution was realized in the axial (arterial radial) direction using the phases of ultrasonic echoes. However, the ultrasonic field does not oscillate in the lateral (arterial longitudinal) direction and, thus, the spatial resolution is degraded compared with that in the axial direction. Such degradation of the lateral spatial resolution depends on the lateral point spread function (PSF) of the employed ultrasound system. In the present study, a method using a Wiener filter was proposed for the suppression of the effect of PSF, and the effectiveness of the proposed method was validated using a phantom. Then, the proposed method was applied to the in vivo measurement of carotid arteries.

2. Principles

2.1 Measurement of surface roughness of arterial wall

Figure 1 shows the displacement of the arterial wall during a cardiac cycle. In a fixed ultrasonic beam, the axial (z-axis) displacement is detected when the luminal surface is rough and the arterial wall moves in the arterial longitudinal (lateral) direction.[19] In addition, the arterial wall also moves in the arterial radial (axial) direction owing to expansion of the artery caused by an increase in blood pressure during a cardiac cycle. As described above, the axial displacement
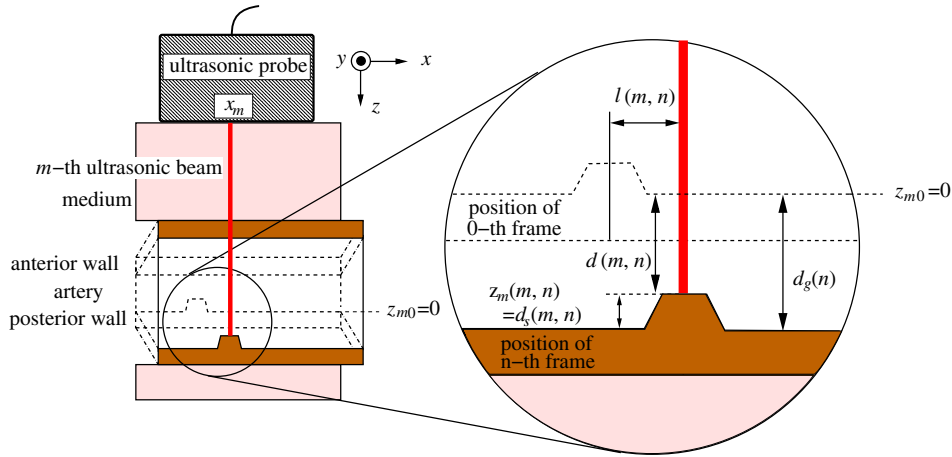
Fig. 1. (Color online) Illustration of displacement of arterial wall between 0-th and n-th frames.

estimated by the ultrasonic phased-tracking method[20–22] in a fixed ultrasonic beam includes displacements caused by surface roughness and arterial expansion.

In Fig. 1, the lateral position of the m-th ultrasonic beam is denoted by x_m ($x_m = m \cdot \delta x$, where δx is the spacing between ultrasonic beams). The axial (z-axis) displacement of the posterior wall surface $\Delta d(x_m, n) \equiv \Delta d(m, n)$ between the n-th frame [t (s)] and the $(n+1)$-th frame [$(t + \Delta T)$ (s)] (ΔT: frame interval) obtained by the phased-tracking method is expressed by the difference between the axial positions $z(x_m, n) \equiv z(m, n)$ and $z(x_m, n+1) \equiv z(x, n+1)$ in the n-th and $(n+1)$-th frames as

$$\Delta d(m, n) = z(m, n+1) - z(m, n). \qquad (1)$$

The total displacement $\widehat{d}(m, n)$ measured by the phased tracking method contains both the global displacement of the arterial wall $\widehat{d_g}(n)$ due to the expansion of the artery and the displacement $\widehat{d_s}(m, n)$ due to the surface roughness as follows:

$$\widehat{d}(m, n) = \widehat{d_g}(n) + \widehat{d_s}(m, n). \qquad (2)$$

The width of the measured region is much smaller than the length of the pulse wave. Therefore, the global wall motion between the n-th and $(n+1)$-th frames at positions $\{x_m\}$ ($m = 0, 1, 2, \ldots, M-1$) are assumed to be the same. The instantaneous axial displacement $\Delta \widehat{d_g}(n)$ caused by global wall motion can be estimated by averaging the axial instantaneous displacements $\{\Delta \widehat{d}(m, n)\}$ as follows:

$$\widehat{d_g}(n) = \sum_{l=0}^{n} \Delta \widehat{d_g}(l), \qquad (3)$$

$$\Delta \widehat{d_g}(n) = \frac{1}{M} \sum_{m=0}^{M-1} \Delta \widehat{d}(m, n), \qquad (4)$$

where M is the number of ultrasonic beams.

Finally, the surface profile $z_m(x; z_{m0})$ measured at the m-th ultrasonic beam is expressed as follows:

$$\widehat{z}_m(x; z_{m0}) \equiv \widehat{z}_m(x_m + \widehat{l}(m, n); z_{m0})$$
$$= z_{m0} + \sum_{n=0}^{n} \Delta \widehat{d_s}(m, n), \qquad (5)$$

$$\Delta \widehat{d_s}(m, n) = \Delta \widehat{d}(m, n) - \Delta \widehat{d_g}(n), \qquad (6)$$

where z_{m0} is the initial height.

The arterial longitudinal displacement $l(m, n)$ should be estimated by the block matching technique[23–25] with reconstructive interpolation[26–28] to obtain the surface profile $z_m(x; z_{m0})$ as a function of the lateral position $x = x_m + l(m, n)$. Furthermore, several surface profiles $\{z_m(x; z_{m0})\}$ were measured in multiple ultrasonic beams $\{m\}$ and combined to obtain a surface profile in a wider region. The proposed method using a Wiener filter, which will be described in the subsequent section, was applied to the combined surface profile for the improvement in the lateral spatial resolution.

2.2 Improvement in lateral spatial resolution using Wiener filter

A measured surface profile can be expressed by the convolution of the true surface profile and the lateral point spread function of an ultrasound system. In diagnostic ultrasound imaging, the Wiener filter is used for the improvement in the spatial resolution of a B-mode ultrasonic image.[29–34] In the present study, the Wiener filter was used for the improvement in the spatial resolution in the measurement of a minute surface roughness. Figure 2 shows a block diagram illustrating how to estimate the true surface profile $\hat{f}(x)$ from the surface profile $g(x)$ measured by ultrasound using the Wiener filter $M(\omega_x)$, where $\hat{F}(\omega_x)$ and $G(\omega_x)$ are the spatial frequency spectra of $\hat{f}(x)$ and $g(x)$, respectively, where ω_x is the spatial angular frequency in the lateral direction. In Fig. 2, $H(\omega_x)$, $N(\omega_x)$, and $F(\omega_x)$ are the spatial frequency spectra of the lateral PSF, noise, and true surface profile, respectively.

The Wiener filter $\hat{M}(\omega_x)$ is determined so as to minimize the mean squared difference between the spectrum of the true surface profile $F(\omega_x)$ and its model $\hat{F}(\omega_x)$. The estimate $\hat{F}(\omega_x)$ is given by

$$\hat{F}(\omega_x) = G(\omega_x) \cdot M(\omega_x)$$
$$= \frac{G(\omega_x) \cdot H_j^*(\omega_x)}{|H(\omega_x)|^2 + P_N(\omega_x)/P_F(\omega_x)}, \qquad (7)$$

where $P_N(\omega_x)$ and $P_F(\omega_x)$ are the average power spectra of

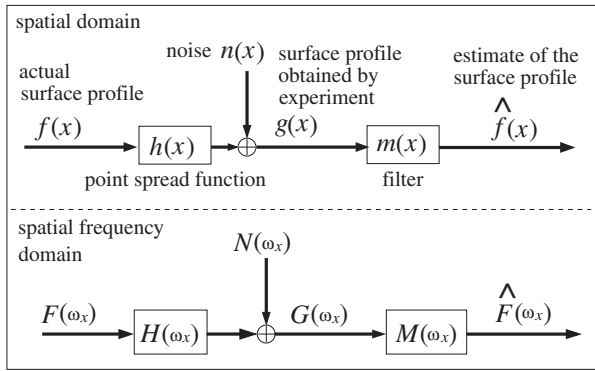**Fig. 2.** Block diagram of the procedure for obtaining estimate $\hat{F}(\omega_x)$ using Wiener filter $M(\omega_x)$.

Fig. 3. (Color online) Illustration of experimental setup for measurement of PSF.

the noise $N(\omega_x)$ and the true surface profile $F(\omega_x)$, respectively.[35–39]

In the present study, the point spread function $h(x)$ was identified by measuring the surface profile of a phantom, in which a fine wire was placed on a flat surface of a silicone rubber plate as described in next section. Regarding $P_N(\omega_x)$, the phantom was measured A times, and the measured profiles $\{g_i(x)\}$ $(i = 0, 1, 2, \ldots, A-1)$ were averaged. The difference between the measured surface profile $\{g_i(x)\}$ and the average surface profile $\bar{g}(x)$ were defined as the noise $\{n_i(x)\}$, and $P_N(\omega_x)$ was calculated by averaging the magnitudes of the spatial frequency spectra $\{N_i(\omega_x)\}$ of the noise $\{n_i(x)\}$ as follows:

$$\bar{G}(\omega_x) = \frac{1}{A}\sum_{i=1}^{A} G_i(\omega_x) = \hat{H}(\omega_x) \tag{8}$$

$$N_i(\omega_x) = G_i(\omega_x) - \bar{G}(\omega_x) \tag{9}$$

$$P_N(\omega_x) = \frac{1}{A}\sum_{i=1}^{A} |N_i(\omega_x)|^2. \tag{10}$$

Regarding $P_F(\omega)$, the same phantom was also measured A times using laser. The power spectrum of the true surface profile $P_F(\omega)$ was estimated by averaging the magnitudes of the spatial frequency spectra $\{F_i(\omega_x)\}$ of the surface profile $\{f_i(x)\}$ measured using laser as follows:

$$P_F(\omega) = \frac{1}{A}\sum_{i=1}^{A} |F_i(\omega_x)|^2. \tag{11}$$

In the present study, the weighting function $P_N(\omega)/P_F(\omega)$ determined in the basic experiment was also applied to in vivo measurement.

2.3　Determination of Wiener filter

To estimate the PSF in the lateral direction $H(\omega_x)$ and the weighting function $P_N(\omega_x)/P_F(\omega_x)$ in the Wiener filter $M(\omega_x)$, a phantom consisting of a fine wire (diameter: 15 μm), which can be considered as a point scatterer, placed on a flat surface of a silicone rubber plate was measured. Ultrasonic diagnostic equipment (Hitachi-Aloka SSD-6500) with a 10 MHz linear array probe was used for the acquisition of beamformed RF signals. Figure 3 shows the experimental setup.

The surface profile $g(x)$ of the phantom was measured 10 times by the method presented in Ref. 19 by moving the
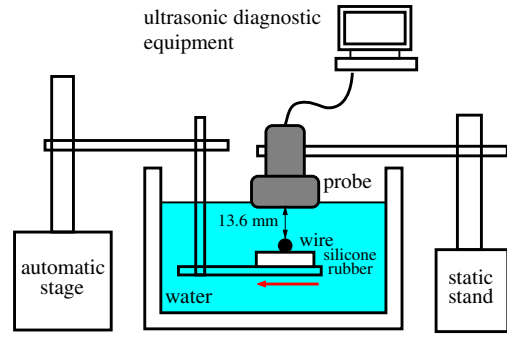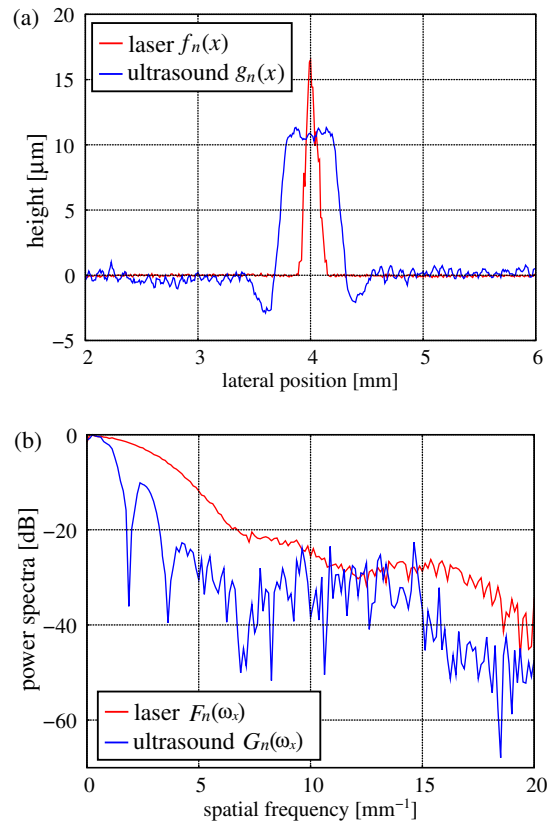

Fig. 4. (Color online) Experimental results of measurement of fine wire for determination of PSF. (a) Surface profiles measured using ultrasound and laser. (b) Spatial power spectra of measured surface profiles.

ultrasonic probe in the lateral direction using an automatic stage. The frequency spectra $\hat{H}(\omega_x)$ and $P_N(\omega_x)$ were estimated by applying the Fourier transform to the mean and standard deviation of the surface profiles $\{g(x)\}$ for the 10 measurements. Also, $P_F(\omega_x)$ was obtained by applying the Fourier transform to the surface profile of the phantom measured by a laser displacement meter (Keyence LT-9010 and LT-9000). In the laser measurement, the surface profile of the phantom was also scanned using an automatic stage. Measurements were also conducted 10 times for the laser measurements. Figures 4(a) and 4(b) show the surface profiles measured using ultrasound and laser and the power spectra of the measured surface profiles, respectively. Using the results shown in Fig. 4, the Wiener filter $M(\omega_x)$ was

determined using the average power spectra of the surface profiles measured using ultrasound as the estimated point spread function $\hat{H}(\omega_x)$.

2.4 Control parameter β used for weighting function

The relative magnitude of the weighting function $P_N(\omega_x)/P_F(\omega_x)$ to the PSF $H(\omega_x)$ should be determined to appropriately control the effect of the proposed Wiener filter $M(\omega_x)$. The Wiener filter $M(\omega_x)$ behaves as an inverse filter $1/H(\omega_x)$ when the signal-to-noise ratio (SNR) is high. On the other hand, if SNR is low, the effect of the Wiener filter $M(\omega_x)$ is suppressed. Conventionally, a real constant is used to control the contribution of the weighting function $P_N(\omega_x)/P_F(\omega_x)$. This can be carried out by multiplying $P_N(\omega_x)/P_F(\omega_x)$ by a real constant β.[40–42] A smaller control parameter, $\beta (\geq 0)$, is preferred in order to improve the spatial resolution at the expense of a noise increment. In the conventional Wiener filter, $\beta = 1.0$. On the other hand, the filter works as an inverse filter at every spatial frequency when β is low, corresponding to the assumption of a high SNR at all spatial frequencies. In such a case, noise contained at a high spatial frequency tends to be amplified, although a higher spatial resolution is realized. To determine the optimum value of the control parameter, the RMSE between the surface profile $\hat{f}(x)$ measured by ultrasound and the true surface profile $f(x)$ measured using laser was calculated for $\{\beta\}$ values of 0–1. The magnitude of the PSF $|H(\omega_x)|$ was normalized to limit the range of the control parameter β from 0 to 1 as follows:

$$H(\omega_x)|_{\text{normalized}} = \frac{1}{\sqrt{\sum\limits_{\omega_x=0}^{\omega_n} |H(\omega_x)|^2}} \cdot H(\omega_x), \qquad (12)$$

where ω_n is a Nyquist angular frequency. Using this optimal control parameter β_{opt}, the proposed Wiener filter is defined as follows:

$$M(\omega_x) = \frac{H^*(\omega_x)|_{\text{normalized}}}{|H(\omega_x)|_{\text{normalized}}|^2 + \beta_{\text{opt}} \cdot \dfrac{P_N(\omega_x)}{P_F(\omega_x)}}. \qquad (13)$$

2.5 Determination of control parameter β

To determine the optimum control parameter β, another phantom made of silicone rubber, which has a minute sawtooth shape (the height of each teeth is 12 µm), was measured using both ultrasound and laser. Figure 5 shows the experimental setup for ultrasonic measurements. To simulate the motion of the carotid arterial wall, the phantom was moved in both axial and lateral directions by an automatic stage, and the probe was fixed by a fixed stand. RF echoes were sampled at 40 MHz for 1.4 s during the movement of the phantom by ±1.0 and ±0.5 mm in the lateral and axial directions, respectively. The frame rate and lateral intervals between beams were 169 Hz and 100 µm, respectively.

Figure 6 shows a B-mode image of the phantom, and the surface profile measured by ultrasound before the application of the proposed Wiener filtering is shown in Fig. 7 (green line). The surface profile was also measured using laser (red line in Fig. 7) by moving the laser displacement meter in the lateral direction using an automatic stage. In Fig. 7, the surface profile obtained by applying the proposed Wiener
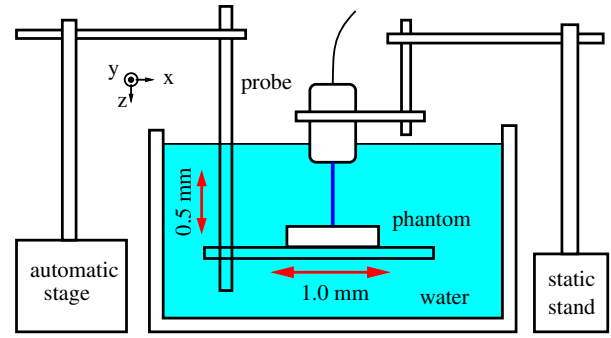

Fig. 5. (Color online) Illustration of experimental setup for ultrasonic measurement of surface roughness using a phantom.
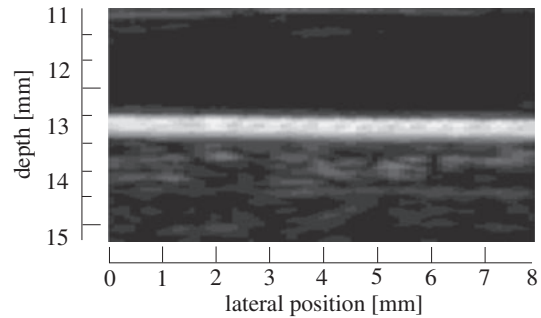

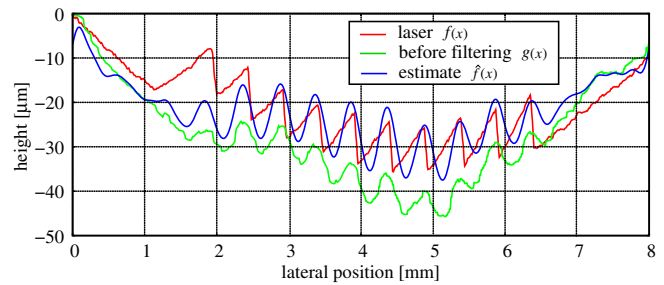**Fig. 6.** B-mode image of a silicone phantom with sawtooth shape.

Fig. 7. (Color online) Results of measured surface profile of a phantom (red line: true surface profile measured by laser; green line: surface profile before application of the filtering; and blue line: estimated surface profile after application of the filtering).

filter with the optimum control parameter β_{opt} is also shown by the blue line.

To determine the optimal control parameter β_{opt}, the root mean square errors (RMSEs) between true surface profile measured by laser $f(x)$ and the estimated surface profiles $\{\hat{f}(x)\}$ were evaluated at $\{\beta\}$ values of 0–1. In Fig. 8, RMSE is plotted as a function of the control parameter β, and the optimum control parameter β_{opt} was determined to be 0.036.

The power spectra of the measured surface profile $g(x)$ and the estimate $\hat{f}(x)$ are shown in Fig. 9(a). The Wiener filter $M(\omega_x)$ and the weighting function $P_N(\omega_x)/P_F(\omega_x)$ are also shown in Figs. 9(b) and 9(c), respectively. The signal-to-noise ratio (SNR) was higher in the spatial frequency range of 0–5 mm^{-1}, and the proposed Wiener filter worked as an inverse filter mainly in this spatial frequency range.

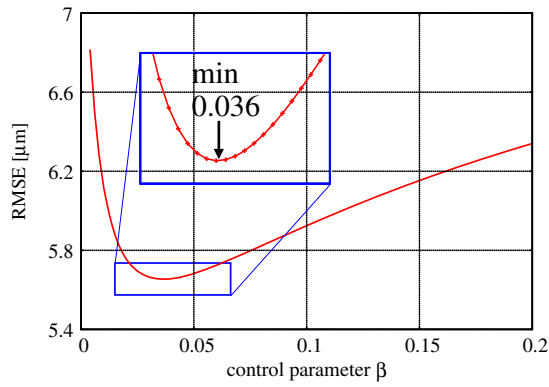**Fig. 8.** (Color online) Root mean square errors between the measured and true surface profiles plotted as a function of control parameter β.
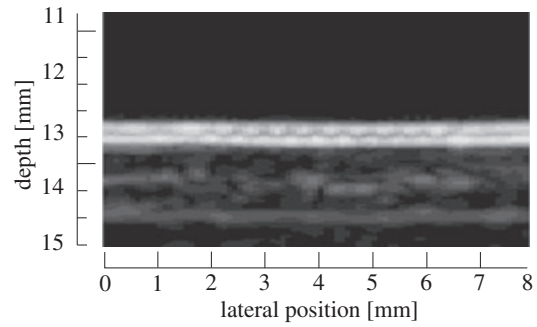

Fig. 10. B-mode image of phantom in the presence of a porcine cutlet between ultrasonic probe and phantom.
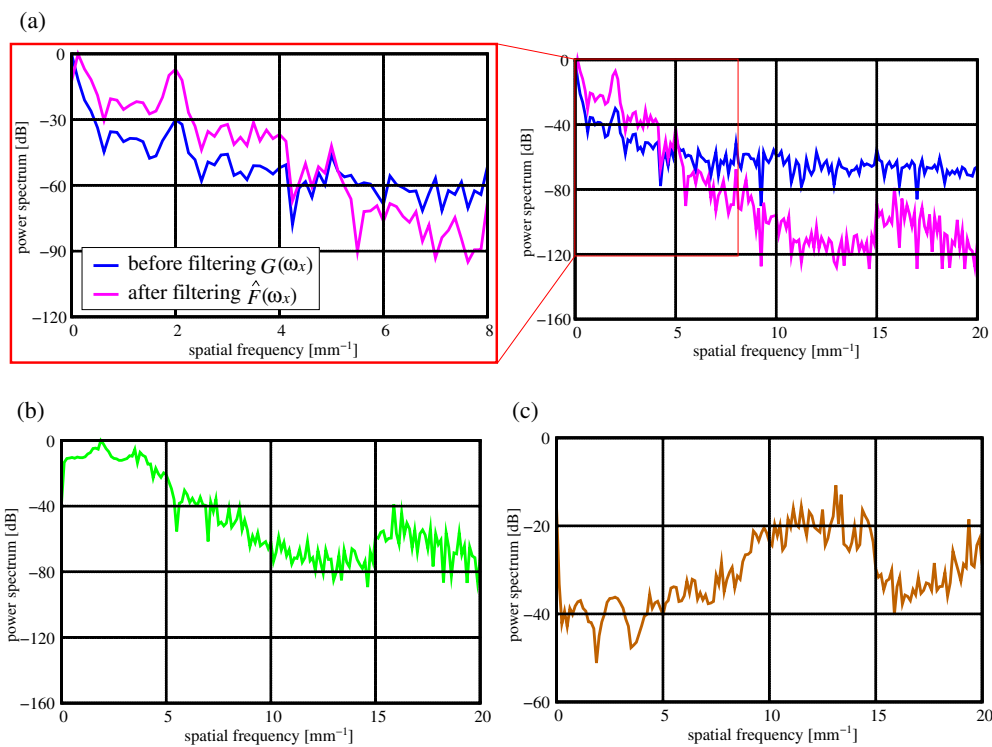

Fig. 9. (Color online) (a) Power spectra of surface profiles pre- and post-filtering ($\beta_{opt} = 0.036$). (b) Power spectrum of designed Wiener filter. (c) Power spectrum of the weighting function.

3. Experimental results

3.1 Basic experiments

Under the condition for in vivo measurements, there is a medium with a nonuniform sound velocity distribution between the skin and the carotid anterior wall. Therefore, the phantom was measured under the condition that a porcine cutlet, which simulated soft tissue, was placed between the ultrasonic probe and the phantom. The system for this experiment was the same as that shown in Fig. 5 except for the porcine cutlet (the thickness of the cutlet was about 10 mm). A B-mode image of the phantom is shown in Fig. 10. Figure 11 shows the measured surface profiles. As shown in Fig. 11, the surface profile became sharper and the height of each sawtooth became closer to that obtained using laser by our method with the proposed Wiener filter. Even in

the presence of an inhomogeneous propagating medium between the ultrasonic probe and the target, the minute surface profile can be measured accurately. In this measurement, the weighting function $P_N(\omega_x)/P_F(\omega_x)$ and the control parameter β, which were determined in basic experiments described in Sects. 2.3 and 2.5, respectively, were used.

In the present study, the control parameter β and the weighting function $P_N(\omega_x)/P_F(\omega_x)$ were determined by basic experiments and, thus, RF echoes acquired in those experiments contain a smaller noise than that obtained in the in vivo measurement. Therefore, the proposed filter may not work appropriately under a low-SNR condition and may lead to the appearance of false peaks in the estimated surface profile $\hat{f}(x)$. To investigate the effect of SNR on the proposed filter, the SNR of the acquired ultrasonic echo signal was varied by adding white noise to the ultrasonic echo signal in
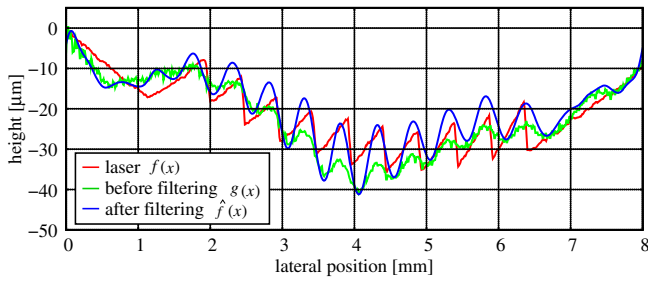
Fig. 11. (Color online) Measurement of surface profile of phantom with porcine cutlet (red line: true surface profile measured by laser; green line: surface profile before application of the filtering; and blue line: estimated surface profile after application of the filtering).

Fig. 12. (Color online) Surface profiles of a phantom estimated under different SNRs of ultrasonic echo signal. (a) SNRs from 25.0 and 27.1 dB. (b) SNRs from 22.0 and 24.0 dB. (c) SNRs from 19.0 and 21.0 dB. The SNR of the ultrasonic echo signal without additional white noise is 27.1 dB.

the data analysis. White noise was generated using MATLAB (MathWorks, U.S.A.), and its amplitude was controlled by multiplying it by a variable constant. The SNR was evaluated using the envelope $s_{m,n}(t)$ of the ultrasonic RF signal in the m-th beam and n-th frame as follows:

$$\text{SNR} = \frac{\frac{1}{M}\sum_{m=1}^{M}\frac{1}{L}\sum_{l=1}^{L}[\bar{s}_m(t+lT_s)]}{\frac{1}{M}\sum_{m=1}^{M}\frac{1}{L}\sum_{l=1}^{L}\left[\frac{1}{N}\sum_{n=1}^{N}[s_{m,n}(t+lT_s)-\bar{s}_m(t+lT_s)]^2\right]},$$
(14)

where $\{\bar{s}_m(t)\}$ is the average of $\{s_{m,n}(t)\}$ for N frames, L is the number of RF echo signals in the depth direction, corresponding to the length of the correlation window used in the *phased-tracking method*, and T_s is the sampling interval. Figure 12 shows the estimated surface profiles, while changing the SNR.

Figures 13(a) shows the RMS difference between the surface profile obtained at each SNR and that measured using laser. Figure 13(b) shows the RMS difference between the surface profile obtained at each SNR and that obtained from the ultrasound echo signal without additional white noise (corresponding to an SNR of 27.1 dB). As shown in Fig. 12, the RMS difference between the results obtained using ultrasound and laser includes the differences in both the sawtooth shape and global shape of the surface profile, and it is difficult to consider the effect of the SNR using the RMS difference between the results obtained using ultrasound and laser. Therefore, in the present study, the effect of the SNR was discussed using the difference of the results obtained with and without the additional white noise shown in Fig. 13(b).

As shown in Fig. 12, the height of the sawtooth decreases significantly when the SNR was lower than 20 dB. Therefore, an SNR of more than 20 dB is required for the proposed filtering method. However, note that a peak in the lateral position of 1–2 mm was separated at an SNR of 20 dB, as shown in Fig. 12(c), even though the height of each sawtooth does not change significantly. Such deformation of the surface profile possibly occurs under an SNR of 20 dB.

3.2 Results of in vivo experiments
Ultrasonic RF data were obtained from carotid arteries of three healthy subjects [subject A (23-year-old healthy male),
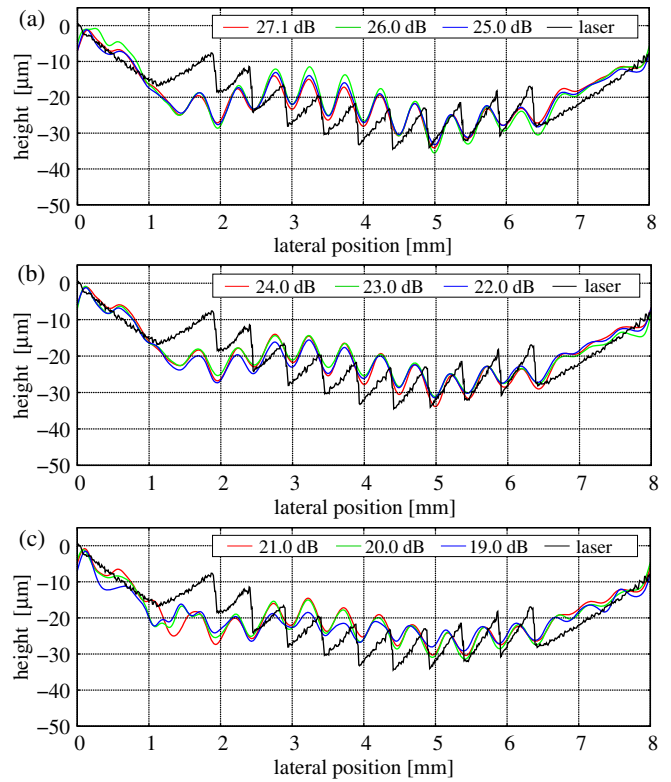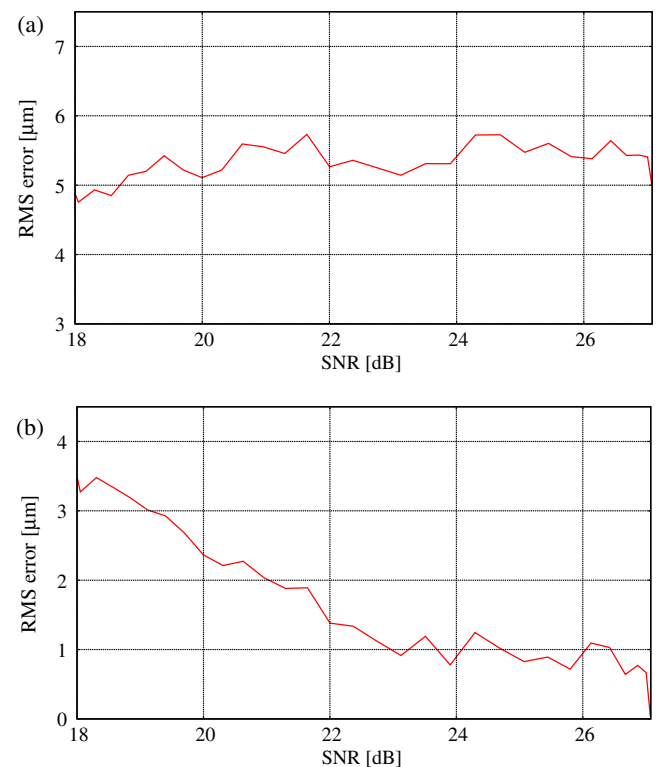

Fig. 13. (Color online) (a) RMS difference between surface profile estimated under each SNR and that measured by laser. (b) RMS difference between surface profile estimated with additional white noise and that estimated without additional white noise.
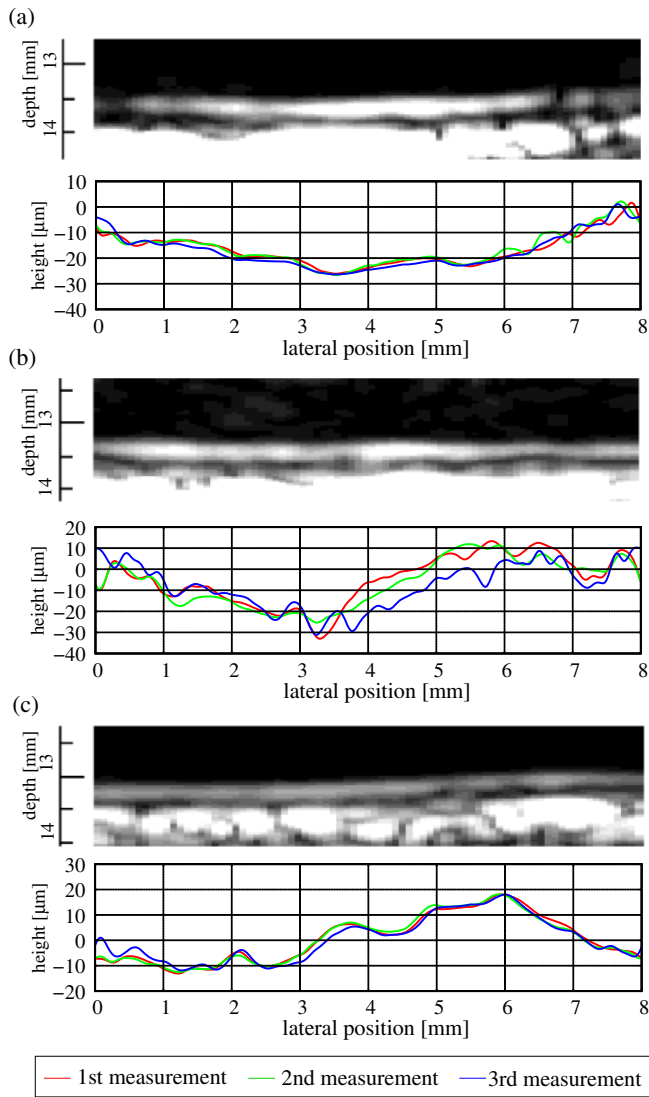
(a)

(b)

(c)

— 1st measurement   — 2nd measurement   — 3rd measurement

Fig. 14. (Color online) B-mode images of carotid arteries and estimated luminal surface profile after the application of the proposed filtering obtained from (a) subject A (23-year-old healthy male), (b) subject B (23-year-old healthy male), and (c) subject C (24-year-old healthy male).

subject B (23-year-old healthy male), and subject C (24-year-old healthy male)] for three cardiac cycles. Figures 14(a)–14(c) show B-mode images of the carotid arterial walls of the respective subjects. The frame rate was set at 165 Hz. In the measurements, RF data were also acquired using a 10 MHz linear probe, which was the same as that used in the basic experiment. Using our method with the proposed Wiener filtering method, the profiles of luminal surfaces were estimated for three cardiac cycles, as shown in Fig. 14. The optimum control parameter β_{opt} of 0.036 was used. From Fig. 14, we confirmed that minute luminal surface profiles of carotid arteries could be estimated reproducibly for each subject. The SNRs of the ultrasonic echo signals in in vivo measurements shown in Fig. 14 were 22.2 dB (subject A), 20.2 dB (subject B), and 24.8 dB (subject C), which were over 20.0 dB. Figure 15 shows the luminal surface profiles before and after the application of the proposed Wiener filtering method obtained from the first measurement for all the subjects (a: subject A, b: subject B, c: subject C).

4. Discussion

In the present study, the PSF of the employed ultrasound system was identified by measuring a fine wire placed on a flat surface of a silicone rubber plate. Figure 16 shows the power spectra of the surface profiles of the fine wire measured using laser (red line) and ultrasound (blue line), the PSF estimated by averaging the power spectra obtained from the ultrasound measurements (green line), and the product of the power spectrum of the surface profile of the fine wire measured using laser and the power spectrum of PSF (pink line). By assuming the power spectrum measured using laser as the true value, the product of the spectra of the true profile and PSF corresponds to the power spectrum obtained by the ultrasonic measurement. The power spectrum of the product of the spectra of the true profile and PSF was suppressed in the spatial frequency range over about $4 \, \text{mm}^{-1}$. The PSF was measured in water, and the noise could be neglected. Therefore, the effect of the proposed Wiener filter was suppressed in the spatial frequency range of over $4 \, \text{mm}^{-1}$ because the difference between the power spectrum obtained by the ultrasonic measurement and the product of spectra of the true profile and PSF, which corresponds to noise components, was significant in that spatial frequency range.

In addition, the optimal control parameter was determined by evaluating the RMSEs of the estimated surface profile from the true surface profile shown in Fig. 7. However, the RMSEs contained not only the error in each estimated sawtooth shape but also that in the global shape of the phantom. Therefore, there is a possibility that the determined optimum control parameter is not the best value to realize a high spatial resolution, which should minimize the error in each estimated sawtooth shape. To determine the optimal control parameter, it would be better to use a simple phantom, which, for example, has a single minute rectangular shape on its surface, to reduce the error caused by the global surface shape of a phantom. In addition, in Figs. 7 and 11, false peaks appeared around a lateral position of 1.3 mm in the estimated surface profile $\hat{f}(x)$ obtained using the proposed filter. Although no significant false peak was found in the in vivo experimental results, the suppression of these false peaks should be investigated in the future task. Also, it should be confirmed that the proposed filter works appropriately when other phantoms with different surface profiles are used.

In in vivo measurements, the surface profiles of the three healthy subjects were measured reproducibly. The standard deviations (SDs) of the surface profiles measured three times each for subjects A, B, and C were calculated as 1.1, 3.8, and 1.0 μm, respectively. The SD in subject B was larger than those in subjects A and C. The reason for this could be considered that the amplitude of RF echoes from the luminal surface of the carotid arterial wall of subject B was low and the echoes could not be obtained stably during a cardiac cycle. For example, in the regions of 0–1 and 6.5–8 mm in Fig. 12(a) (subject A), the dispersion of the estimated surface profiles became larger and the accuracy of the measurement was degraded.

Furthermore, for the quantitative evaluation of the luminal surface roughness, the root mean square roughness (R_q) would be useful. The calculated root mean square rough-
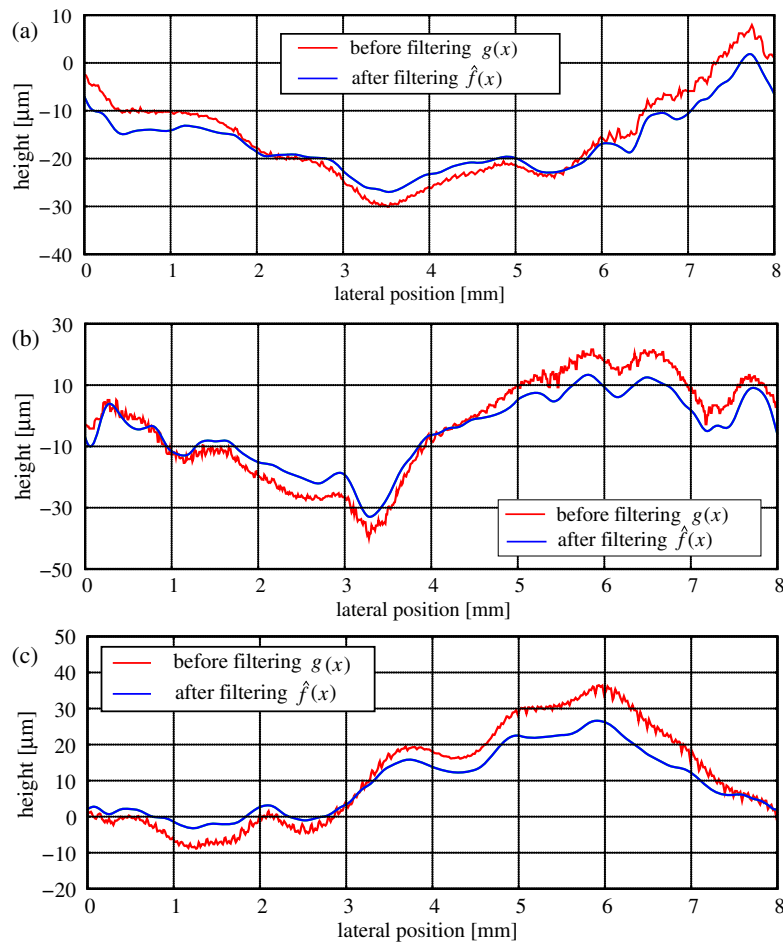
Fig. 15. (Color online) Surface profiles before and after application of the proposed Wiener filtering obtained from the first measurement (blue line: surface profile after application of the filtering; red line: surface profile before application of the filtering). (a) Subject A. (b) Subject B. (c) Subject C.
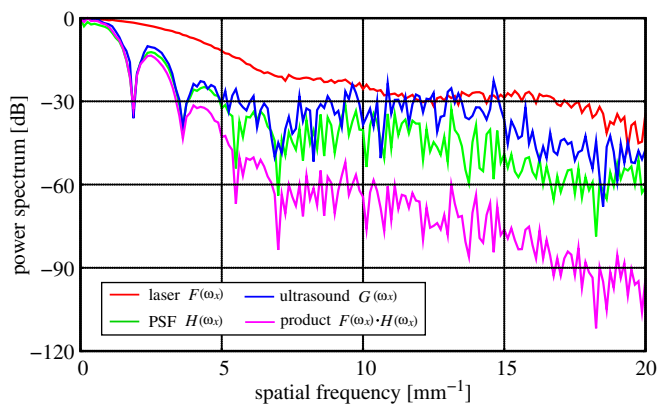

Fig. 16. (Color online) Power spectra of surface profiles measured by laser (red line), ultrasound (blue line), PSF (green line), and product of power spectra of true surface profile and PSF (pink line).

nesses $\{R_q\}$ were 8.1, 10.6, and 8.1 μm for subjects A, B, and C, respectively. The R_q values were about 10 μm. However, it is expected that, in the measurement of subjects suffering from atherosclerosis, R_q is expected to become larger than those of the healthy subjects shown in the present study.

5. Conclusions

In the present study, a method using a Wiener filter was proposed to improve the spatial resolution in the measurement of the minute luminal surface profile of the carotid arterial wall. The point spread function of the employed ultrasound system was determined by measuring a fine wire for designing the Wiener filter. Also, to determine the optimum parameter, which controls the effect of the Wiener filter, the root mean square error between the surface profile of a phantom measured by ultrasound and the true surface profile measured using laser was evaluated. By applying the identified Wiener filter to the measured surface profile of the phantom, we confirmed that the spatial resolution of the measurement of the surface profile was improved. Furthermore, the proposed method was applied to in vivo ultrasound data obtained from the carotid arteries of three healthy subjects. We confirmed that minute luminal surface profiles could be estimated reproducibly. These results show that a micron-order minute roughness can be estimated more accurately using the proposed filtering method.

1) K. Ikeshita, H. Hasagawa, and H. Kanai, Jpn. J. Appl. Phys. **47**, 4165 (2008).
2) K. Ikeshita, H. Hasagawa, and H. Kanai, Jpn. J. Appl. Phys. **48**, 07GJ10 (2009).
3) K. Ikeshita, H. Hasagawa, and H. Kanai, Jpn. J. Appl. Phys. **50**, 07HF08 (2011).
4) K. Ikeshita, H. Hasagawa, and H. Kanai, Jpn. J. Appl. Phys. **51**, 07GF14 (2012).
5) J. Persson, J. Formgren, B. Israelsson, and G. Berglund, Arterioscler. Thromb. Vasc. Biol. **14**, 261 (1994).

6) D. S. Celermajer, K. E. Sorensen, V. M. Gooch, D. J. Spiegelhalter, O. I. Miller, and I. D. Sullivan, Lancet **340**, 1111 (1992).
7) N. Ibrahim, H. Hasagawa, and H. Kanai, Jpn. J. Appl. Phys. **51**, 07GF07 (2012).
8) N. Ibrahim, H. Hasagawa, and H. Kanai, Jpn. J. Appl. Phys. **52**, 07HF03 (2013).
9) E. Sho, M. Sho, T. M. Singh, H. Nanjo, M. Komatu, C. Xu, H. Masuda, and C. K. Zarins, Exp. Mol. Pathol. **73**, 142 (2002).
10) R. Ross, New Engl. J. Med. **340**, 115 (1999).
11) A. Schmidt-Trucksäss, M. Sandrock, D. C. Cheng, H. M. Müller, M. W. Baumstark, R. Rauramaa, A. Berg, and M. Huonker, Atherosclerosis **166**, 57 (2003).
12) M. Sandrock, C. Schulze, D. Schmitz, H.-H. Dickhuth, and A. Schmidt-Trucksaess, Br. J. Sports Med. **42**, 839 (2008).
13) A. Krebs, A. Schmidt-Trucksäss, J. Wagner, K. Krebs, J. Doerfer, and K. O. Schwab, Pediatr. Diabetes **6**, 161 (2005).
14) Y. Uehara, I. Saito, T. Kushiro, and F. Nakamura, *Hitomede Wakaru Kekkann Shogai* (Vascular Disorders at a Glance) (MEDSI, Tokyo, 1995) [in Japanese].
15) C. Arihara, H. Hasegawa, and H. Kanai, Jpn. J. Appl. Phys. **45**, 4727 (2006).
16) M. Cinthio, Å. R. Ahlgren, T. Jansson, A. Eriksson, H. W. Persson, and K. Lindström, IEEE Trans. Ultrason. Ferroelectr. Freq. Control **52**, 1300 (2005).
17) M. Cinthio, H. Hasegawa, and H. Kanai, IEEE Trans. Ultrason. Ferroelectr. Freq. Control **58**, 853 (2011).
18) M. Cinthio, H. Hasegawa, and H. Kanai, IEEE Ultrasonics Symp., 2007, p. 997.
19) K. Kitamura, H. Hasegawa, and H. Kanai, Jpn. J. Appl. Phys. **51**, 07GF08 (2012).
20) H. Kanai, M. Sato, Y. Koiwa, and N. Chubachi, IEEE Trans. Ultrason. Ferroelectr. Freq. Control **43**, 791 (1996).
21) H. Kanai, K. Sugimura, Y. Koiwa, and Y. Tsukahara, Electron. Lett. **35**, 949 (1999).
22) H. Kanai, Y. Koiwa, and J. Zhang, IEEE Trans. Ultrason. Ferroelectr. Freq. Control **46**, 1229 (1999).
23) S. Golemati, A. Sassano, M. J. Lever, A. A. Bharath, A. Dhanjil, and A. N. Nicolaides, Ultrasound Med. Biol. **29**, 387 (2003).
24) J. H. Velduis and G. W. Broudland, Image Vision Comput. **17**, 905 (1999).
25) K. Kitamura, H. Hasegawa, and H. Kanai, Tech. Rep. IEICE **41**, 383 (2011) [in Japanese].
26) I. Cespedes, Y. Huang, J. Ophir, and S. Spratt, Ultrason. Imaging **17**, 142 (1995).
27) Y. Honjo, H. Hasegawa, and H. Kanai, Jpn. J. Appl. Phys. **49**, 07HF14 (2010).
28) Y. Honjo, H. Hasegawa, and H. Kanai, Jpn. J. Appl. Phys. **51**, 07GF06 (2012).
29) S. Kageyama, H. Hasegawa, and H. Kanai, Jpn. J. Appl. Phys. **52**, 07HF04 (2013).
30) T. Taxt and J. Strand, IEEE Trans. Ultrason. Ferroelectr. Freq. Control **48**, 861 (2001).
31) S. Wan, B. I. Raju, and M. A. Srinivasan, IEEE Trans. Ultrason. Ferroelectr. Freq. Control **50**, 1286 (2003).
32) C. P. Loizou, C. S. Pattichis, C. I. Christodoulou, R. S. H. Istepanian, M. Pantziaris, and A. Nicolaides, IEEE Trans. Ultrason. Ferroelectr. Freq. Control **52**, 1653 (2005).
33) W.-S. Yeoh and C. Zhang, IEEE Trans. Biomed. Eng. **53**, 2001 (2006).
34) O. Michailovich and A. Tannenbaum, IEEE Trans. Image Process. **16**, 3005 (2007).
35) A. Rosenfeld and A. C. Kak, *Dhijitaru Gazoshori* (Digital Image Processing) (Kindai Kagaku, Tokyo, 1978) [in Japanese].
36) W. K. Pratt, *Digital Image Processing* (Wiley, New York, 1978).
37) H. C. Andrew and B. R. Hunt, *Digital Image Restoration* (Prentice Hall, Upper Saddle River, NJ, 1997).
38) M. Saito, *Dhijitaru Gazoshori* (Digital Image Processing) (Tokai University Press, Hiratsuka, 1986).
39) J. Jan, *Medical Image Processing, Reconstruction and Restoration: Concepts and Method* (CRC Press, Boca Raton, FL, 2005).
40) S. Måsøy, T. F. Johansen, and B. Angelsen, J. Acoust. Soc. Am. **113**, 2009 (2003).
41) S. Hantscher, A. Reisenzahn, and C. G. Diskus, IET Rader Sonar Navig. **2**, 315 (2008).
42) J. R. Fienup, D. K. Griffith, L. Harrington, A. M. Kowalczyk, J. J. Miller, and J. A. Mooney, Proc. SPIE **4792**, 452396 (2002).